Title: Thermo-mechanical pressurization of experimental faults in cohesive rocks during seismic slip

Authors: Violay, M.[1,2*], Di Toro, G.[3,4], Nielsen, S.[5], Spagnuolo, E.[6], Burg, J.P.[1]

Affiliations:

[1] ETH D-ERDW, Sonnegstrasse, 5 CH-8092, Zürich, Switzerland

[2]EPFL-ENAC, LEMR, Station 18 CH-1015, Lausanne, Switzerland

[3] Dipartimento di Geoscienze, Università degli Studi di Padova, Via G. Gradenigo 6, 35131, Padua, Italy

[4] School of Earth, Atmospheric & Environmental Sciences, University of Manchester, Oxford Road, Manchester M13 9PL, UK

[5] Earth Sciences Department, University of Durham, South Road, Durham DH13LE, UK

[6] Instituto Nazionale di Geofisica e Vulcanologia, Via di Vigna Murata 605, 00143, Rome, Italy

Correspondence to: marie.violay@epfl.ch

Highlights:

High velocity friction experiments on cohesive rocks under undrained conditions

Experimental evidence of thermo-mechanical pressurization (TMP)

TMP weakening of cohesive rocks is negligible during earthquakes

Keywords:

Friction, earthquakes, fluids, thermo-mechanical pressurization, basalt, marble

Abstract:

Earthquakes occur because fault friction weakens with increasing slip and slip rates. Since the slipping zones of faults are often fluid-saturated, thermo-mechanical pressurization of pore fluids has been invoked as a mechanism responsible for frictional dynamic weakening, but experimental evidence is lacking. We performed friction experiments (normal stress 25 MPa, maximal slip-rate ~3 ms^{-1}) on cohesive basalt and marble under (1) room-humidity and (2) immersed in liquid water (drained and undrained) conditions. In both rock types and independently of the presence of fluids, up to 80% of frictional weakening was measured in the first 5 cm of slip. Modest pressurization-related weakening appears only at later stages of slip. Thermo-mechanical pressurization weakening of cohesive rocks can be negligible during earthquakes due to the triggering of more efficient fault lubrication mechanisms (flash heating, frictional melting, etc.).

Introduction

During earthquakes, few millimeters thick slip zones within fluid-saturated, cohesive or non-cohesive rocks are sheared over several meters (80 m for the Tohoku 2011 Mw 9.0 earthquake, **Fujiwara et al., 2011**) at slip rates of meters per second and under normal stresses up to hundreds of MPa (**Sibson, 1973; Rice, 2006**). The frictional power per unit area (product of the slip rate per frictional shear stress, in the range of 1-100 MW m^{-2}) is dissipated as heat and rock fragmentation in the slipping zone (**Sibson, 1980**). This large power triggers several mechano-chemical processes that may induce frictional weakening (**Di Toro et al., 2011; Goldsby and Tullis, 2011; Reches and Lockner, 2010**). Thermo-mechanical pressurization (TMP) of pore fluids trapped is one of the possible processes responsible for fault dynamic weakening (**Sibson, 1973; Rice,1992; 2006; Lachenbruch, 1980; Brantut et al., 2010; Bizzari and Cocco, 2006; Segall and Rice, 2008; Wibberley and Shimamoto, 2005**). Given the widespread presence of fluids in natural slipping zones, TMP has been

thoroughly investigated from a theoretical point of view. TMP models are based on two competing processes: fluid and rock expansion in response to shear heating and the fluid storage capacity of the rock (**Rice, 2006; Segall and Rice, 2008; Platt et al., 2014**).

Several experimental studies were carried on to investigate TMP (**Mizoguchi et al., 2009; Brantut et al., 2008; Ferri et al., 2010; 2011; De Paola et al., 2011; Mitchell et al., 2015; Faulkner et al., 2011; Ujiie et al., 2011; 2013)**. Experiments approached seismic deformation conditions by imposing slip rates (V) of ~1 ms^{-1}, slip (δ) up to tens of meters, and effective normal stresses (σ_n^{eff}) of tens of MPa on clay-, calcite- and dolomite-rich gouges under room-humidity and wet conditions. The measured large weakening (up to 80-90% of friction drop at 1 ms^{-1}) was attributed to: (1) in part (< 20%) thermochemical pressurization associated to the breakdown of clays and release of H_2O (**Brantut et al., 2008; 2010; Ferri et al., 2010**) or to the breakdown of calcite and dolomite and release of CO_2 (**De Paola et al., 2011; Mitchell et al., 2015**) in the case of room-humidity experiments and, (2) thermal pressurization in the case of wet experiments on clay-rich gouges (**Faulkner et al., 2011; Ferri et al., 2010; Ujiie et al., 2011; 2013**). However, technical issues related to fluid and gouge confinement impeded measuring the pore fluid pressure in the sample chamber. We installed on the rotary shear machine SHIVA (Slow-to-High-Velocity-Apparatus, INGV Rome, **Suppl. Material S1**) an on-purpose designed pressure-vessel that allows shearing cohesive rocks immersed in fluids and to measure the pore fluid pressure during the experiments (**Violay et al., 2013**). Previous experiments were performed under drained conditions on Carrara marbles and gabbros (**Violay et al., 2013; 2014**). We report new results obtained by shearing basalts and Carrara marbles under undrained conditions. Though the actual experimental configuration does not allow shearing saturated gouges, the results for cohesive rocks are intriguing: the contribution of TMP during shearing of cohesive rocks at

74 seismic slip rates is negligible compared to the contribution from other weakening
75 mechanisms.
76
77 **Material and methods**
78 To investigate seismic slip in the presence of pore fluids, 33 friction experiments
79 (**Table 1)** were conducted at room temperature on hollow cylinders (50/30 mm
80 external/internal diameter) of Etna basalt (Electron Micro-Probe Analysis reported in **Table**
81 **2**) and Carrara marble (99.9% calcite, X-Ray Diffraction and X-Ray Fluorescence analysis,
82 **Violay et al., 2013**). Samples were jacketed with aluminium rings, sealed with epoxy to
83 prevent fluid leaks and inserted in the fluid pressure vessel (**Nielsen et al., 2012**; **Suppl.**
84 **Material S1**). The description of SHIVA (**Di Toro et al., 2010; Niemeijer et al., 2011**) and
85 of the experimental configuration used to perform experiments with pressurized fluids can be
86 found in **Suppl. Material S1**. The main difference with respect to previous studies conducted
87 with fluids (**Violay et al., 2013; 2014**) was the disposition of the closed valves, which
88 allowed imposing undrained conditions (see **Suppl. Material S1** for full description**)**.
89 Experiments were performed (1) under room-humidity conditions and immersed in water, (2)
90 drained conditions (the specimen is saturated and continuously connected to the water
91 reservoir, (**Paterson and Wong, 2005)**, resulting in constant fluid pressure and preventing
92 fluid pressurization) and (3) undrained conditions (the specimen was first saturated and then
93 isolated from the water reservoir: fluid pressurization was induced by reduction in pore
94 volume, (**Paterson and Wong, 2005)** and by increase in fluid volume due to thermal
95 expansion during shearing). A K-Type thermocouple was inserted at about 3 mm from the
96 slip surface of the sample to measure the temperature evolution of the fluid during the
97 experiments. The thermocouple was installed in the "stationary side" (i.e., normal stress
98 loading column) of SHIVA.

Experiments were performed by spinning two rock cylinders at accelerations of 7.8 ms^{-2}, V = 3 ms^{-1}, 4 m < δ < 8 m, normal stress (σ_n) from 15 to 35 MPa and initial fluid pressure $P_f(t_0)$= 5 MPa (**Violay et al., 2013; 2014**). Mechanical data (axial load, torque, slip, angular rotation) were acquired at a frequency up to 25 kHz. δ, V and shear stress (τ) were determined using methods described in **Di Toro et al.** (2010), **Niemeijer et al.,** (2011) and **Tsutsumi and Shimamoto** (1997). The two rock-types were selected because are common crustal rocks and for their relatively low porosity (< 5%) and low permeability (< $10^{-17}m^2$) (e.g., **Vinciguerra et al., 2005**). The slip zones of experiments conducted on basalts could be recovered because the two rock cylinders were welded by glass due to the solidification of the frictional melt produced during shearing. The microstructures were investigated with an optical microscope and electron probe micro-analyzer (JEOL, JXA-8200 at ETH, Zurich). The chemical compositions of grains and glasses were determined on carbon-coated, polished thin sections using an Electron Probe Micro-Analyzer (EPMA) JEOL, JXA-8200 (ETH, Zurich) with a focused beam about 1 μm in diameter under accelerating voltage of 15 kV and current 15 nA. The slipping zones of experiments conducted on Carrara marble could not be recovered *in-situ* (only few dispersed remnants were found) because they consisted of non-cohesive material that was flushed away during the ejection of the fluid from the vessel after the experiment.

Results

Mechanical data

Experiments performed under identical ambient and deformation conditions resulted in systematically reproducible mechanical data for both Etna basalt and Carrara marble (**Figs. 1-4**). We present the measurements of the friction for comparison with data obtained at

different initial effective normal stresses and the measurements of the shear stress for comparison of data obtained at a given imposed initial effective normal stress (all mechanical data are summarized in **Table 1**). We define the friction coefficient based on effective normal stress ($\mu = \tau / \sigma_n^{eff}(t)$ or Terzaghi's principle for $\sigma_n^{eff}(t) = \sigma_n(t) - \alpha P_f(t)$ with α =1, incorporating instantaneous σ_n and P_f). However, since $P_f(t)$ varies during the experiment due to effect of thermal expansion, to illustrate more clearly the effect of TMP we also present the results in Fig. 4 based on the initial value of $P_f(t_0)$ alone ($\mu = \tau / \sigma_n^{eff\text{-}0}(t)$ with $\sigma_n^{eff\text{-}0}(t) = \sigma_n(t) - P_f(t_0)$).

For Etna basalt, the coefficient of friction decayed almost exponentially from a peak value μ_p=0.59±0.08 at about slip initiation (i.e., 0.64±0.05 for room humidity conditions, 0.58±0.05 for drained and 0.53±0.07 for undrained conditions) to a steady-state value μ_{ss} that decreased with increasing effective normal stress (**Figs. 1 and 4**). The μ_{ss} was determined from the average value of friction coefficient (μ) between 4.5 and 5.5 meters slip, except for experiment s921 where μ_{ss} was determined between 2.5 and 3.5 meters slip. The initial decay of the friction coefficient (and thus of the shear stress) was similar independently of the ambient conditions (**Fig. 3**). At $\sigma_n^{eff}(t_0)$= 20 MPa (i.e. σ_n^{eff} *at the initiation of the experiment)*, the residual friction coefficient after 5 cm of slip ranged from μ_{r_5cm} = 0.20-0.25 for the room humidity (s485 and s541), to μ_{r_5cm} = 0.26-0.28 for the drained (s921 and s926) and to μ_{r_5cm} = 0.22-0.24 for the undrained (s922, s925, s927 and s933) experiments (**Table 1**). The μ_{r_5cm} corresponded to a percentage of friction drop with respect to μ_p (or $\%\Delta\mu = 100\ (\mu_{r\_5cm} - \mu_{ss})/(\mu_p - \mu_{ss})$) ranging from 80.2% (s485, room humidity conditions), to 56.4% (s921, drained conditions) **(Fig. 4, and Table 1)**. Given the larger μ_p in room humidity experiments, the drop in percentage of the friction coefficient in the first 5 cm of slip was slightly larger in room humidity conditions (73.06±5.24%) than in both drained (67.96±8.36%) and undrained (68.35±3.65%) conditions (**Fig. 4**).

Instead, the steady-state shear stress ($\tau_{ss,}$ was determined from the average value of shear stress between 4.5 and 5.5 meters slip, except for experiment s921 where τ_{ss} was determined between 2.5 and 3.5 meters slip) was about 20% lower under undrained than under drained and room-humidity conditions, for similar V, δ, and initial $\sigma_n^{eff}(t_0)$(**Figs. 2, 3, Suppl. Material S2**). For instance, at initial $\sigma_n^{eff}(t_0)$= 20 MPa, the coefficient of friction decayed from a peak value μ_p = 0.55∓0.07 (corresponding to a shear stress of 11±1.4 MPa) towards a steady-state value μ_{ss} = 0.11∓0.01 (shear stress of 2.2±0.2 MPa) under room-humidity conditions, μ_{ss} = 0.11∓0.01 (shear stress of 2.2±0.2 MPa) under drained conditions and μ_{ss} = 0.09∓0.01 (shear stress of 1.8±0.2 MPa) and under undrained conditions (**Table 1; Fig. 2**). Under undrained conditions, an overpressure *dP* (such that $P_f = P_f(t_0) + dP$, *(with $P_f(t_0)$ the fluid pressure at the initiation of the experiment*) was measured with increasing slip (**Fig. 2A**) following a power law best fitted by $dP = 8.4\ (\mp 0.6)\ \delta^{0.2(\mp 0.07)}$ [MPa] (for σ_n= 25 MPa, V= 3 ms^{-1} $P_f(t0)$=5 MPa). Overpressure *dP* decreased immediately by ~60% after the slip was stopped (**Fig. 2A).** Conversely, P_f and σ_n did not vary under drained conditions (**Fig. 2A**). Sample shortening rate was constant and almost negligible during the first five centimetres of slip for both drained and undrained conditions (**Fig.3B**). For slip longer than 5 cm, the shortening rate was ~0.170 mm/m and ~0.089 mm/m in drained and undrained conditions, respectively **(Fig.1, Table 1).**

For Carrara marble, the friction coefficient evolved from μ_p= 0.60±0.07 to μ_{ss}= 0.04±0.02 **(Table 1)**. Contrary to Etna basalt, τ_{ss} and shortening rate were almost negligible and similar (~0.0001 mm/m) under room humidity, drained and undrained conditions, even if a small pore fluid overpressure (*dP* ~1 MPa) was measured after several meters of slip under undrained conditions (**Fig. 2B**). The μ_{r_5cm} was larger (and similar) for both undrained

(68.96±1.79%) and drained (70.44±2.58%) conditions, than under room humidity (49.85±4.39%) conditions (**Table 1; Fig. 4D**).

Temperature measurement

The maximum temperature measured by the thermocouple immersed in the fluid was 35 ºC for experiment s929 performed at normal stress of 25 MPa, initial fluid pressure of 5 MPa, target slip rate of 3 ms^{-1} and total slip of 6 m **(Fig. 5).** The thermocouple measured the temperature evolution with time of the water in the pressure vessel due to the frictional heat generated and diffused from the slip surface. Because of heat diffusion in water, the thermal perturbation was detected with some delay with respect to the initiation of the experiment. This renders the determination of the temperature of the sliding surface a complicated task.

Microstructures

After the experiments and irrespective of the ambient conditions, in Etna basalt, a continuous 100-200 μm thick layer of glassy-like material separated the rock cylinders **(Fig. 6)**. Under the optical microscope, the layer was homogeneous and brown coloured in parallel-polarized light, and extinct in cross-polarized light, suggesting that the layer was made of solidified friction melt (i.e., glass). This interpretation is consistent with the observed extrusion of drops of melt during experiments performed at room-humidity conditions, and with the presence, in all experiments, of a lump of glassy-like material preserved in the inner hole of the hollow cylinders. The electron microprobe analysis showed that, independently of the environmental conditions and in all of the experiments where steady-state friction was achieved, the glass had a chemical composition almost identical to the bulk composition of the initial basalt **(Table 2).** From image analysis of FE-SEM microphotographs, the glassy-like layer of experiments performed under room-humidity contained < 1% in volume of

vesicles and ~16 ± 5% in volume of lithic clasts (< 10 μm in size); instead, in experiments performed in the presence of fluids, the glassy-like layer contained 3±2% in volume of vesicles and ~9±3 % in volume of lithic clasts (< 10 μm in size) in both drained and undrained conditions **(Fig. 6).**

For Carrara marble, in room-humidity experiments performed at $\sigma_n^{eff}(t_0)$ = 20 MPa, δ= 4÷7 m and V = 3 ms^{-1} s, the wall rocks were separated by ~100 μm thick continuous slip zone composed of fine-grained (< 50 nm in size) non-cohesive material (see Fig. 5 in **Violay et al., 2013**). In drained and undrained experiments, the compacted gouge layers were not investigated because they could not be found on the slip zone.

Discussion

In the two rock types under both room-humidity and drained conditions, μ_p and μ_{ss} were consistent with those previously measured in basaltic **(Violay et al., 2014)** and carbonate-bearing rocks **(Han et al., 2007; 2010; Violay et al., 2013)**. Comparing room-humidity and drained experiments shows that water had almost no effect on μ_p and μ_{ss} **(Figs. 2-4) (Violay et al., 2014**). However, for Etna basalt, experiments performed under undrained conditions **(Fig. 2)** had about 20% reduction of τ_{ss} compared to room-humidity and drained experiments. Moreover, the fluid pressure increased with slip under undrained conditions, but was constant under drained conditions **(Fig. 2)**. This is further supported by a temperature increase of 35ºC measured by the thermocouple immersed in the fluid of undrained experiments **(Fig. 5),** and < 5ºC in drained experiments (for $\sigma_n^{eff}(t_0)$ = 20 MPa, δ = 6 m and V = 3 ms^{-1}). The undrained thermal pressurization coefficient defined as the pore pressure increase for a unit temperature increase ranges from 0.01 MPa/°C to 0.1 MPa/°C **(Ghabezloo and Sulem, 2009).** An increase in bulk temperature of 35ºC of the fluid results in an increase in pore pressure of 0.35–3.5 MPa. We interpret the reduction of τ_{ss} to result from TMP within

223 the slipping zone. The measured shear stress reduction is consistent with the melt lubrication
224 model of **Nielsen et al. (2008)** according to which the rate of extrusion of friction melt from
225 the slipping zone is regulated by the difference between the viscous pressure of the melt and
226 the normal stress acting on the fault. Although the Terzaghi's principle cannot be applied
227 under melt-lubricated conditions, we may draw a parallel about the role of the effective
228 normal stress: the increase in fluid pore pressure in the slipping zone limits the melt extrusion
229 rate from the slipping zone in the same way as the decrease of the normal stress acting on the
230 fault. In both cases, the bulk result is the reduction of the viscous shear stress. This is
231 confirmed by the sample shortening rate lower under undrained (e.g., 0.089 mm/m) than
232 drained (0.17 mm/m) conditions **(Fig. 2A and Table 1)**. Under undrained conditions, after the
233 slip stopped, part of the pressurization dP in excess of $P_f(t_0)$gradually decreased **(Fig. 2A)**.
234 This indicates that *thermal* pressurization due to water thermal expansion during frictional
235 heating was dropping upon cooling of the water (by conduction through the vessel metal. A
236 residual *mechanical* pressurization endured after cooling, due to the permanent volume
237 reduction in connection to sample shortening. The fluid in the inner chamber of the hollow
238 cylindrical rock specimen is hydraulically isolated from the external chamber which was
239 directly connected to the pressurizing system (**Suppl. Material S1**). During sample
240 shortening, the fluid trapped in the central hallow of the specimen may exert spurious fluid
241 pressures. However, the contribution of fluid pressure from the inner hollow was negligible
242 during the experiments. In fact:
243 1) in Carrara marble, the Terzaghi's principle was satisfied assuming the imposed fluid
244 pressure is the fluid pressure measured on the annular sample (**Violay et al., 2013**);
245 2) in basalt, the sample shortens faster in drained (e.g., s926) than in undrained (e.g., s925)
246 conditions (**Fig. 2A**). As a consequence, experiments performed under drained conditions
247 would result in larger reduction of the volume of the inner chamber and, being the inner

chamber hydraulically isolated, in higher (spurious) pore pressures. The bulk effect would be a lower measured shear stress in drained conditions than in undrained conditions, which is the opposite of what we measured (τ_{ss} is lower under undrained conditions, **Fig. 2A**);

3) similar experiments performed on solid cylinders (i.e., without the central hollow chamber) of gabbro under drained and undrained conditions resulted in τ_{ss} lower under undrained than drained conditions, confirming results obtained with hollow specimens (**Suppl. Material S2**).

As a consequence the effect of the fluid pressure from the inner chamber (central hallow) on the axial load is negligible, and the axial cavity does not count as part of the simulated fault area. Indeed, all experimental results (e.g. peak friction value) are consistent with an effective normal stress (σ_n-α P_f) where the normal stress σ_n is axial force normalized by the annular slip area only (e.g., **Violay et al., 2013; 2014**). The small to negligible contribution in fluid pressure during axial shortening from the fluid trapped in the inner hollow is due its epoxy filling. Epoxy is compliant and deforms during sampling shortening, buffering the increase in fluid pressure in the cavity.

In spite of the evidence of a measurable TMP, we question whether it is an efficient fault weakening mechanism during seismic slip, in particular in the presence of more rapid and effective alternative mechanisms. Under undrained conditions, fluid overpressures of ~1 MPa and 0.05 MPa were measured after 5 cm of slip for Etna basalt and Carrara marble, respectively (**Figs. 2A-B; 3A**). The initial overpressure (dP) was associated to a relative (dP *100/τ_p) apparent shear stress drop of maximum 10% for $\sigma_n^{eff}(t_0)$=20 MPa in Etna basalt (squared dots in **Fig. 4**), and no shear stress drop in Carrara Marble. Since the shear stress drop was 65-80% after 5 cm of slip for both lithologies, more efficient lubricating mechanisms may have been activated at the initiation of slip and at steady-state. Elasto-hydrodynamic lubrication or weakening induced by the overpressure generated by the shear of a thin viscous fluid comprised between two sub-parallel and rough surfaces (**Brodsky and**

273 **Kanamori, 2001**) may be excluded, as discussed in **Violay et al. (2013**). Cavitation or the
274 formation of vapour-filled cavities in a flowing liquid due to rapid changes in pressure may
275 also be excluded. When cavities implode, they produce intense fluid pressure variations that
276 induce accelerated erosion of the solid surface and high levels of noise. However, there is (1)
277 no evidence of abrupt variations in fluid pressure or normal stress in both drained and
278 undrained conditions (see **Figs. 2 and 3A**) and (2) no intensification of surface erosion (wear)
279 in experiments performed with fluids with respect to room-humidity (**Fig. 3B**). Moreover,
280 acoustic emissions were recorded in experiments conducted with SHIVA but on Westerly
281 granite in room-humidity and drained conditions (**Passelegue et al., 2013**). Noteworthy, the
282 intensity and number of acoustic emissions increased in room-humidity conditions (i.e., in the
283 absence of liquid water) suggesting that cavitation did not occur in the presence of pore fluids.
284 At the initiation of slip in both marble and basalt, the negligible contribution of TMP
285 to the large frictional weakening of the experimental fault is further supported by the absence
286 of variations in either normal stress or shortening (i.e. no evidence of dilatation) (**Fig. 3B**).
287
288 At steady-state, the ineffectiveness of TMP is demonstrated by **1)** the occurrence of solidified
289 friction melts, which cover the surface of Etna Basalt cylinders independently of the fluid
290 content. The experimental and microstructural observations suggest that the dominant
291 weakening mechanism was flash heating causing melting at asperity contacts at the initiation
292 of slip and frictional melt lubrication at steady-state **(Goldsby and Tullis, 2011, Brown and**
293 **Fialko, 2012, Violay et al., 2014)** and **2)** the occurrence of ultrafine-grained material in water
294 for Carrara marble experiments, independently of the hydraulic conditions. The experimental
295 and microanalytical observations suggest that the dominant weakening mechanism in Carrara
296 marble was probably flash heating of asperities at the initiation of sliding **(Violay et al., 2013,**
297 **Spagnuolo et al., subm.)** or a grain-size (possibly water-enhanced) dependent process (super-

298 plasticity) at steady-state **(Verberne et al., 2014; Green et al., 2015; De Paola et al., in**
299 **press.).**
300
301 At the initiation of sliding, the apparently small contribution of measured TMP to fault
302 weakening under drained and undrained conditions might be partly due to the experimental
303 configuration. Indeed, at short time intervals, heating affects only the water volume trapped in
304 the slipping zone (Vol_s ~2 10^{-7} m^3, given the average thickness of ~0.16 mm induced by
305 sample roughness over the 1.25 10^{-3} m^2 of slipping area), which is small compared to the fluid
306 volume in the vessel (Vol_v~5 10^{-6} m^3). For reasonable fault-parallel permeability the water on
307 the slipping zone and in the vessel are connected and pressure is at equilibrium. Then the
308 volume expansion of heated slip-zone water:
309 $$d\mathrm{Vol}_{exp} = \lambda \Delta T \, \mathrm{Vol}_s \qquad \text{Eq. 1}$$
310 is accommodated by the total water volume (λ being the water coefficient of thermal
311 expansion). Assuming roughly constant λ, K (water incompressibility) and total available
312 volume Vol_s+Vol_v (i.e., neglecting volume changes due to compliance of the vessel or of
313 rocks on natural faults), we obtain an upper bound pressurization reached during fault slip:
314 $$dP = K \, d\mathrm{Vol}_{exp}/(\mathrm{Vol}_s+\mathrm{Vol}_v) = K \lambda \Delta T \, \mathrm{Vol}_s/(\mathrm{Vol}_s+\mathrm{Vol}_v) \qquad \text{Eq. 2}$$
315
316 On actual faults the volume of connected water (equivalent to Vol_v) per unit fault surface may
317 be smaller than in the experiment, a condition which is readily extrapolated by reducing Vol_v
318 in equation (1). In order to estimate the maximum contribution of TMP to frictional
319 weakening, we assume Vol_v close to zero. The upper bound for pressurization is thus obtained
320 assuming that (1) the heat produced by frictional sliding is entirely dissipated in a small water
321 volume trapped in the slipping zone (Vol_s), (2) volume changes due to compliance of the
322 vessel or of rocks on natural faults are negligible and (3) the buffering effect of thermal

expansion of water by the connected volume is reduced to zero. Using λ=207 10^{-6} ºC^{-1}, K= 2.1 GPa **(Waples and Waples, 2004),** Vol_v=0 and an estimated temperature increase of 20ºC after a slip of 0.1 m we obtain a maximum pressurization of ~1.1 MPa. The bulk temperature increase in the slipping zone (for $\tau(t) = \mu(t)$ $(\sigma_n(t) - P_f(t))$ was estimated using the heat rate production and solving the 1D diffusion problem (Carslaw and Jaeger, 1959) such that:

$$T(t) = \frac{1}{\rho \cdot Cp \cdot \sqrt{\kappa\pi}} \cdot \int_0^t \frac{1}{2} \cdot \frac{\tau(t') \cdot V(t')}{\sqrt{t - t'}} dt \qquad \text{Eq. 3}$$

(where thermal capacity Cp = 880 J kg^{-1} K^{-1} and 116 J kg^{-1} K^{-1} respectively for calcite and basalt samples, density ρ = 2700 kg m^{-3} and 2900 kg m^{-3} respectively for calcite and basalt sample and thermal diffusivity κ = 1.48 10^{-6} m^2 s^{-1} and 0.21 m^2 s^{-1} respectively for calcite and basalt sample and t is the time need to slip from 0 and 100 mm (**Eppelbaum et al., 2014; Hanley et al., 1978; Waples and Waples, 2004;** for further details see **Violay et al., 2013).** From equations 2 and 3, the thermal pressurization of 1.1 MPa would induce a friction drop of about 15% from peak stress; such a drop was already achieved before 0.01 m of slip, even in drained or room-humidity experiments (**Fig. 3**). As a consequence, upon extrapolation to conditions where the water volume surrounding the fault is negligible, thermal pressurization is less efficient than other weakening mechanisms (e.g., flash weakening and heating of asperities) and would add a further relative weakening to an already lubricated fault. The contribution from thermal pressurization will decrease with increasing fluid connectivity and can be quantified as follows. From Eq. 2, the fluid volume expansion dVol_{exp} due to the temperature increase results in an increase in pore fluid pressure:

$$P_{f(t)} = P_{f(t0)} + K \frac{\lambda \, \Delta T \, Vol_s}{Vol_v + Vol_s} \qquad \text{Eq. 4}$$

346 Weakening due to water pressurization w_p increases with P_f:

347 $$w_p = \frac{\sigma_n - P_f(t)}{\sigma_n - P_{if(t0)}} \qquad \text{Eq. 5}$$

348 and is related to the connected fluid volume (in m^3) per unit fault surface in m^2. A value of
349 $w_p = 1$ corresponds to no contribution to weakening from pressurized fluids (i.e., $P_f = P_f(t_0)$.
350 From **Fig. 7**, the maximum effect of pressurization is a drop by 40% for connected volumes of
351 less than a cubic centimetre per unit fault area (corresponding to 10^{-6} m). For values above 1
352 litre of connected water per unit fault area (corresponding to a water layer of average
353 thickness 1 mm) the pressurization effect is buffered and negligible.
354
355 **Conclusions**
356 We conclude that even extremely thin (< 100 μm) and low permeability (< 10^{-17} m^2
357 slipping zones, may lead to a relatively unimportant TMP of pore fluids during seismic slip.
358 These new experimental results apply to slip surfaces within cohesive rocks where strain
359 localization is instantaneous, resulting in rapid temperature increase of the slipping zone and
360 leading to the activation of other weakening mechanisms **(Rice, 2006, Goldsby and Tullis,**
361 **2011, Di Toro et al., 2010).** In the case of non-cohesive rocks (gouges), strain is distributed
362 within the gouge layer before being localized **(Beeler et al., 1996, Marone et al., 1990,**
363 **Smith et al., 2015)**. These results in a gradual temperature increase during slip and TMP of
364 pore fluids might still be an efficient fault weakening mechanism.
365
366 **References**
367 Beeler N.M., et al., 1996. Frictional behavior of large displacement experimental faults. J.
368 Geophys. Res., 101, 8697-8715

Bizzari, A. Cocco, M, 2006. A thermal pressurization model for the spontaneous dynamic rupture propagation on a three-dimensional fault: 1. Methodological approach. J. Geophys. Res., 111, B05303

Brantut, N., Schubnel, A., Rouzaud J.-N., Brunet F., Shimamoto T., 2008. High-velocity frictional properties of a clay bearing fault gouge and implications for earthquake mechanics, J. Geophys. Res., 113, B10401.

Brantut, N. et al., 2010. Thermochemical pressurization of faults during coseismic slip, J. Geophys. Res., 115, B05314

Brodsky, E.E., Kanamori, H., 2001. Elastohydrodynamic lubrication of faults. J. Geophys. Res. 106, 16357–16374.

Brown K. M., Fialko Y., 2012. Melt welt' mechanism of extreme weakening of gabbro at seismic slip rates. Nature, 488, 638-41

De Paola, N., Hirose, T. Mitchell, G. Di Toro, C. Viti, and T. Shimamoto (2011), Fault lubrication and earthquake propagation in thermally unstable rocks, Geology, 39, 35–38.

De Paola, N., Holdsworth, R.E., Viti, C., Collettini, C., Bullock, R. Can grain size sensitive flow lubricate faults during the initial stages of earthquake propagation, submitted to Earth and Planetary Science Letters.

Di Toro G. et al., 2010. From field geology to earthquake simulation: a new state-of-the-art tool to investigate rock friction during the seismic cycle (SHIVA). Rendiconti Lincei, 21, 95–114

Di Toro G. et al., 2011. Fault lubrication during earthquakes. Nature, 471, 494-498.

Eppelbaum L. et al., Applied Geothermics, Lecture Notes in Earth System Sciences, DOI: 10.1007/978-3-642-34023-9_2 Springer-Verlag Berlin Heidelberg 2014

392 Faulkner D.R., Mitchell T.M., Behnsen J., Hirose T., Shimamoto T. 2011 Stuck in the
393 mud? Earthquake nucleation and propagation through accretionary forearcs Geophysical
394 Research Letters, 38.

395 Ferri F., et al., 2010. Evidences of thermal pressurization in high velocity friction
396 experiments on smectite-rich gouges Terra Nova, 22, 347–353

397 Fujiwara T. et al., 2011. The 2011 Tohoku-Oki Earthquake: Displacement Reaching the
398 Trench Axis. Science, 334, 1240-1240

399 Ghabezloo S., Sulem J., 2009. Temperature induced pore fluid pressurization in
400 geomaterials Rock Mech Rock Eng, 29-43

401 Goldsby D.L., Tullis T.E. 2011. Flash heating leads to low frictional strength of crustal
402 rocks at earthquake slip rates. Science, 334, 216-218.

403 Green, H.W., Shi, F., Bozhilov, K., Xia, G., Reches, Z., 2015. Phase transformation and
404 nanometric flow cause extreme weakening during fault slip. Nature Geoscience,
405 DOI:10.1038/NGEO02436

406 Han R. Hirose, T., Shimamoto T., 2010. Strong velocity weakening and powder
407 lubrication of simulated carbonate faults at seismic slip rates. J. Geophys. Res. 115,
408 B03412

409 Han R., et al., 2007. Ultralow friction of carbonate faults caused by thermal
410 decomposition, Science. 316, 878–881

411 Hanley, E.J., Dewitt, D.P., Roy, R.F., 1978. The thermal diffusivity of eight well
412 characterized rocks for the temperature range 300–1000 K. Eng. Geol. 12, 31–47.

413 Hirose T, Shimamoto T., 2005. Growth of molten zone as a mechanism of slip weakening
414 of simulated faults in gabbro during frictional melting. J. Geophys. Res., 110, B05202

415 Lachenbruch, A.H., 1980. Frictional heating, fluid pressure, and the resistance to fault
416 motion. J. Geophys. Res., 85, 6097–6122.

417 Marone C., Raleigh C.B., Scholz C.H., 1990. Frictional behavior and constitutive
418 modeling of simulated fault gouge. J. Geophys. Res., 95, 7007-7025

419 Mitchell T.M., Smith S.A.F., Anders M.H., Di Toro G., Nielsen S., Cavallo A., Beard
420 A.D. 2015. Catastrophic emplacement of giant landslides aided by thermal
421 decomposition: Heart Mountain, Wyoming Earth Planet. Sci. Lett., 411, 199–207.

422 Mizoguchi, K., Hirose, T., Shimamoto, T. and Fukuyama, E., 2009. High-velocity
423 frictional behavior and microstructure evolution of fault gouge obtained from Nojima
424 fault, southwest Japan. Tectonophysics, 471, 285–296

425 Nielsen, S. et al., 2008. Frictional melt and seismic slip. J. Geophys. Res., 113, B01308.

426 Niemeijer, A. et al., 2011. Frictional melting of gabbro under extreme experimental
427 conditions of normal stress, acceleration, and sliding velocity. J. Geophys. Res., 116,
428 B07404.

429 Passelègue F.X., Spagnuolo, E., Violay, M., Nielsen, S.B., Di Toro, G., Schubnel, A.,
430 2013. Influence of slip rate and normal stress on off-fault damage in high-velocity friction
431 experiments on crustal rocks. , American Geophysical Union Annual Meeting Abstracts
432 with Programme T33C-2651.

433 Paterson, M. S., Wong T.-F., (2005). The brittle field, Second ed., 347, Springer Verlag,
434 Berlin, New York.

435 Platt J. D., Rudnicki J. W., Rice J. R., 2014. Stability and Localization of Rapid Shear in
436 Fluid-Saturated Fault Gouge, 2. Localized zone width and strength evolution, J. Geophys.
437 Res., 119, 4334-4359

438 Reches, Z, Lockner D.A., Fault weakening and earthquake instability by powder
439 lubrication. Nature, 467, 452-455

440 Rice J.R., 2006. Heating and weakening of faults during earthquake slip. J. Geophys. Res,
441 111, B05311

442 Rice JR., 1992. Fault stress states, pore pressure distributions, and the weakness of the
443 San Andreas Fault. In Fault Mechanics and Transport Properties of Rocks, ed. B Evans,
444 Tf Wong, pp. 475–504. London: Academic.

445 Segall, P. & Rice, J.R., 2006. Does shear heating of pore fluid contribute to earthquake
446 nucleation? J. geophys. Res., 111, B09316

447 Sibson R.H., 1973. Interactions between Temperature and Pore-Fluid Pressure during
448 Earthquake Faulting and a Mechanism for Partial or Total Stress Relief, Nature, 243, 66–
449 68

450 Smith S.A.F. Nielsen S., Di Toro G. 2015. Strain localization and the onset of dynamic
451 weakening in calcite fault gouge. Earth Planet. Sci. Lett., 413, 25-36

452 Tsutsumi A., Shimamoto T., 1997. High-velocity frictional properties of gabbro.
453 Geophys. Res. Lett., 24, 699–702

454 Ujiie K., Tsutsumi A., Kameda J.2011. Reproduction of thermal pressurization and
455 fluidization of clay-rich fault gouges by high-velocity friction experiments and
456 implications for seismic slip in natural faults Rick Sibson, Geological Society of London
457 Special Publication, 359, 267–285

458 Ujiie, K., *et al.* 2013, Low coseismic shear stress on the Tohoku-oki megathrust
459 determined from laboratory experiments, Science, 342, 1211–1214.

460 Verberne B.A, et al., 2014. Superplastic nanofibrous slip zones control seismogenic fault
461 friction Science. 346, 1342-1344.

462 Vinciguerra S., et al., 2005. Relating seismic velocities, thermal cracking and permeability
463 in Mt. Etna and Iceland basalts J. Rock Mech., 42900-42910.

464 Violay M. et al., 2012. Pore fluid in experimental calcite-bearing faults: abrupt weakening
465 and geochemical signature of co-seismic processes. Earth Planet. Sci. Lett. 361, 74–84

466 Violay M. et al., 2014. Effect of glass on the frictional behavior of basalts at seismic slip
467 rates, Geophys. Res. Lett. 41, 348-355

468 Violay M. et al., 2014. Effect of water on the frictional behavior of cohesive rocks during
469 earthquakes. Geology. 42, 27-30

470 Waples, D.W., Waples, J.S., 2004. A review and evaluation of specific heat capacities of
471 rocks, minerals, and subsurface fluids. Part 1: Minerals and nonporous rocks. Nat. Resour.
472 Res. 13 , 13–130.

473 Wibberley, C.A.J. Shimamoto T, 2005. Earthquake slip weakening and asperities
474 explained by thermal pressurization. Nature, 436, 689–692.

475

476 **ACKNOWLEDGMENTS**

477 We thank R. Lüchinger (ETH) for thin sections preparation and P. Scarlato (INGV), and E.
478 Reusser (ETH) for laboratory support. We acknowledge S. Vinciguerra and R. Bakker for
479 their help with the experiments. MV and JPB thank the ETH and GDT, SN and ES the ERC
480 grant No 614705 NOFEAR for the financial support.

481

482

FIGURES CAPTIONS:

Figure. 1: Friction coefficient versus slip in Etna basalt. Experiments were performed at slip rate, $V = 3$ ms^{-1} (target slip rate), acceleration = 7.8 ms^{-2}, and initial normal stress ($\sigma_n^{eff}(t_0)$) comprised between 10 MPa and 30 MPa under either drained conditions (experiments s928, s926 and s930), and undrained conditions (s932, s922, and s924). Independently of the initial $\sigma_n^{eff}(t_0)$, a reduction of ~20% of μ_{ss} was measured in the experiments performed under undrained conditions. The regular oscillations (~0.125 m in wavelength) in shear stress in the initial 3-4 meters of slip observed in experiment s932 are interpreted as due to the not perfect alignment of the sheared samples. In fact, the wavelength of the oscillations corresponds to the equivalent sample circumference [π ($r_{external} + r_{internal}$) = 0.1256 m]. The amplitude of the oscillations decreases progressively with cumulated slip due to wear and melting of the sliding surfaces and disappears after 4 m of slip.

Figure 2: Shear stress versus slip in Etna basalt and Carrara marble. Experiments were performed at $V = 3$ ms^{-1} (target slip rate), acceleration = 7.8 ms^{-2}, and initial effective normal stress ($\sigma_n^{eff}(t_0)) = 20$ *MPa* at the initiation of the experiments under following environmental and hydraulic conditions: A) Etna basalt: room-humidity (s485 σ_n= 20 MPa: black curve), pore water under drained conditions (s921 and s926: red and green curve), pore water under undrained conditions (s922, s925, s927 and s933: yellow, orange, purple, and blue curves). B) Carrara marble: room-humidity (s307 σ_n= 20 MPa: black curve), pore water under drained conditions (s1023 and s1035: red and green curve), pore water under undrained conditions (s1024 and s1028: yellow and blue curves). Pore water pressure (full line) and shortening (dashed line) for drained and undrained experiments are depicted with the same colors as the reported shear stress.

Figure 3: Mechanical data. A) Close up of the first 0.05 m of slip of Fig. 1A for experiments s485 (room-humidity, black curve), s922, s933 (drained, purple and blue curves), s921, s926, (undrained, red and green curves). Pore water pressure for drained and undrained experiments are depicted with the same colors as the reported shear stress. B) Normal effective stress and shortening versus slip plot for experiments s485 (room-humidity, black curve), s922, s933 (drained, purple and blue curves), s921 and s926 (undrained, red and green curves).

Figure 4: Summary figure of the mechanical data for Etna basalt (22 experiments, Figs. A and B) and Carrara marble (11 experiments, Figs. C and D) reported in this study. Experiments were performed at V = 3 ms^{-1} (target slip rate), acceleration = 7.8 ms^{-2}, and $P_f(t_0)$ ~5 MPa at the initiation of the drained and undrained experiments. A) Etna basalt: - friction coefficient vs. effective normal stress with respect to the pore fluid pressure at steady-state ($\sigma_n^{eff}(t)=\sigma_n(t) - (P_f(t_0) + dP)$), i.e. total fluid pressure, including variations due to fluid heating and mechanical effects of sample shortening and volume change in the vessel) under room-humidity conditions (green circles), drained conditions (red circles) and undrained conditions. - Blue squares: Friction coefficient vs. effective normal stress with respect to the pore fluid pressure at the initiation of the experiment ($\sigma_n^{eff\text{-}0}(t)=\sigma_n(t) - P_f(t_0)$. The steady-state shear stress data normalized by the normal effective stress at t_0 show a systematic decrease of c. 20% with respect to the steady-state shear stress normalized by the effective stress at steady-state. Therfore, the double faced black arrows highlights the role of thermo-mechanical pressurization.

B) Etna basalts: percentage of residual friction with respect to the steady-state friction after 5 cm of slip vs. effective normal stress under room-humidity conditions (green circles) drained conditions (red circles) and undrained conditions (blue circles). Y axis: μ_p= peak friction, μ_{ss} = steady-state friction, μ_r = residual friction. (C) and (D), case for Carrara Marble. Standard deviation is within the dimension of the symbols.

534 **Figure 5:** Evolution of the shear stress (blue curve) and temperature (red curve) measured by
535 the thermocouple during experiment s929 (undrained conditions).
536
537 **Figure 6:** Slipping zones of Etna basalt after steady-state friction was achieved (>1 m of slip).
538 Experimental conditions: acceleration 7.8 ms^{-2}, initial $\sigma_n^{eff}(to)$= 20 MPa and slip rate, V = 3
539 ms^{-1}. A-B: Room-humidity conditions C-D: Drained conditions. E-F: Undrained conditions.
540 Independently of the environmental conditions, at the end of experiments, the wall rocks were
541 separated by continuous layer of glass. B, D and F are enlargements of the slipping zones.
542 Field emission scanning electron microscope- Backscattered electron images.
543
544 **Figure 7:** Weakening due to water pressurization w_p versus the connected volume per unit
545 fault surface (values of $w_p = 1$ correspond to no weakening). Maximum effect of
546 pressurization is a drop to 40% for connected volumes of less than a cubic centimeter per unit
547 fault area. For values above 1 liter of connected buffering water, the pressurization effect is
548 negligible.
549
550 **Table 1:** Summary of experimental conditions and results. See main text for explanations.
551 C.M. = Carrara marble; E.B.=Etna basalt.
552
553 **Table 2:** Chemical composition of the basalt and of the glass. Chemical bulk composition of
554 the Etna basalt (Giordano and Dingwell, 2003*); Electron MicroProbe Analysis (EMPA)
555 chemical compositions of the initial glass and of the solidified frictional melt. The EPMA
556 analysis do not close to about 100% because only Fe2+ was determined. The S.D. refers to
557 the standard deviation of the EMPA composition of the solidified friction melts.

* Giordano and Dingwell. 2003. Viscosity of hydrous Etna basalt: implications for plinian-style basaltic eruptions. bull Volcanol 65:8-14.

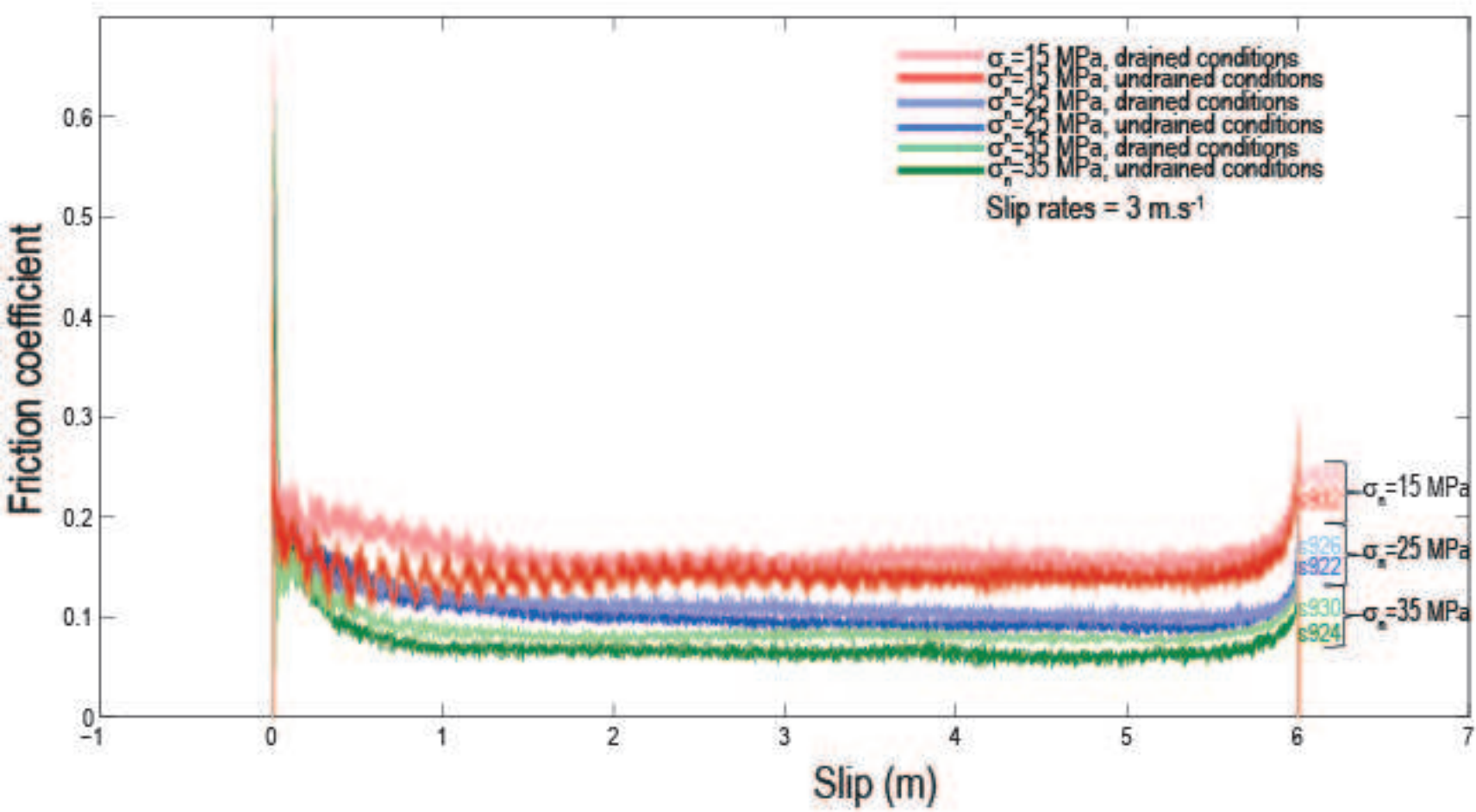
σn=15 MPa, drained conditions
σn=15 MPa, undrained conditions
σn=25 MPa, drained conditions
σn=25 MPa, undrained conditions
σn=35 MPa, drained conditions
σn=35 MPa, undrained conditions
Slip rates = 3 m.s-1
Friction coefficient
Slip (m)
σn=15 MPa
σn=25 MPa
σn=35 MPa
s926
s922
s930
s924

Etna Basalt

$\sigma_n^{eff}(t0)$= 20 MPa
Slip rates = 3 m/s

Drained exp: s921 / s926
Undrained exp: s922 /s925/ s927/ s933
Room humidity exp: s485
Shear stress
Pore pressure
Shortening
Pore Pressure
S926 drained
s925 undrained

Shear Stress (MPa)
Pore fluid pressure (MPa)
Shortening (mm)
Slip (m)

Carrara Marble

$\sigma_n^{eff}(t0)$= 20 MPa
Slip rates = 3 m/s

Drained exp: s1023/ s1035
Undrained exp: s1024/ s1028
Room humidity exp: s307
Shear stress
Pore pressure
Shortening
Pore Pressure
s1028 undrained
s1035 drained

Shear Stress (MPa)
Pore fluid pressure (MPa)
Shortening (mm)
Slip (m)

A) Close up of the first 5 cm of slip in Fig.2a

σ_n^{eff}(t0)= 20 MPa
Slip rates = 3 m/s
Room humidity exp: s485
Drained exp: s921 / s926
Undrained exp: s922 / s933

P_f_s922
P_f_s933
P_f_s926
P_f_s921

Shear Stress (MPa)
Pore fluid pressure (MPa)
Slip (m)

B)

Shortenning
Normal stress

σ_s933
σ_s921
σ_s926
σ_s922
σ_s485

Shortening (mm)
Normal stress (MPa)
Slip (m)

Etna basalt

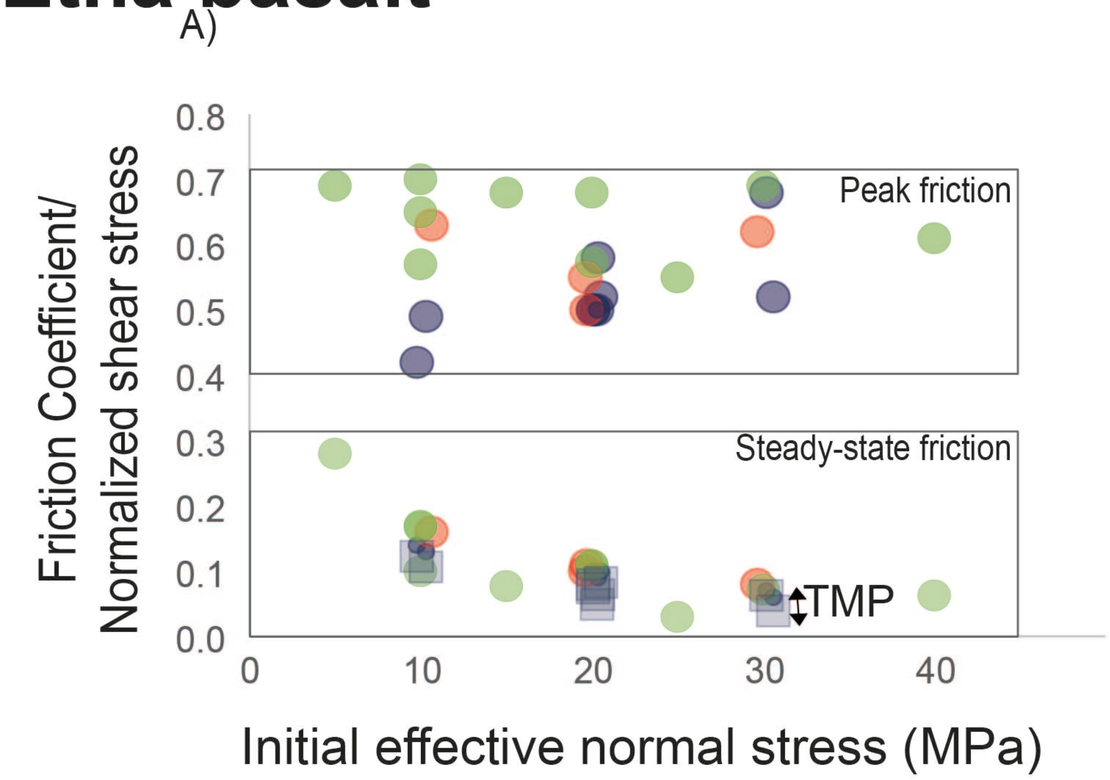

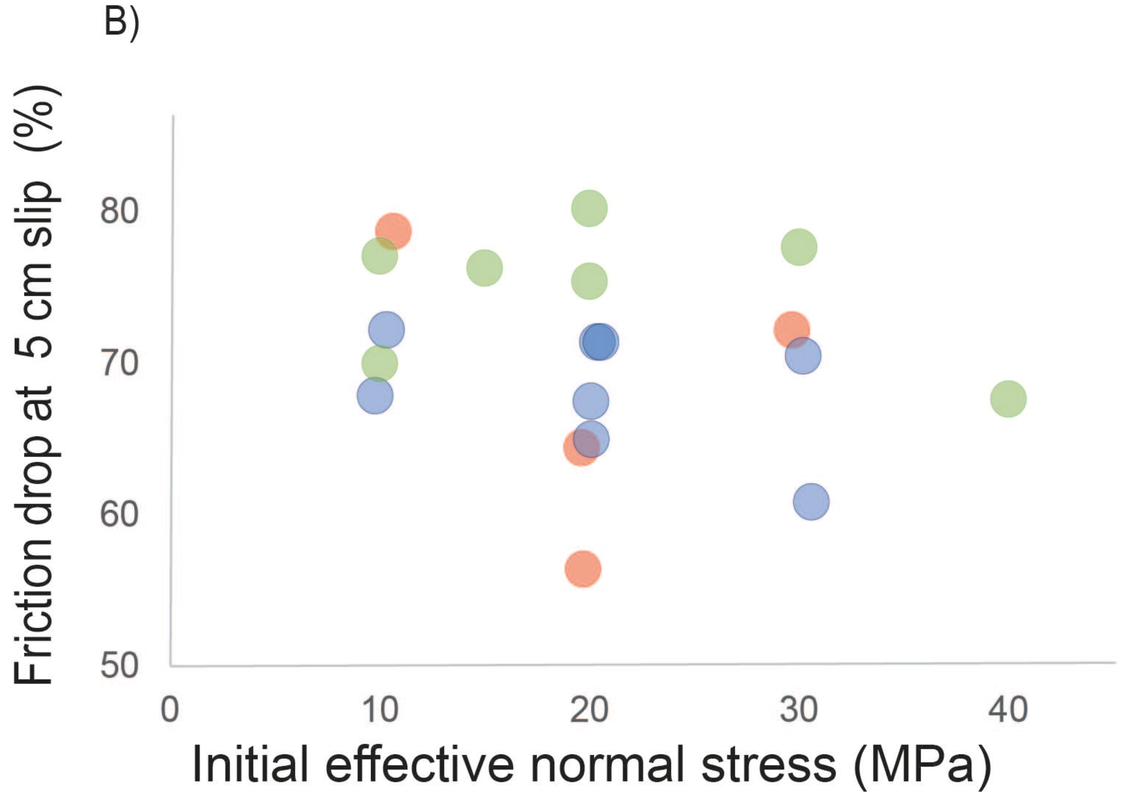

Carrara marble

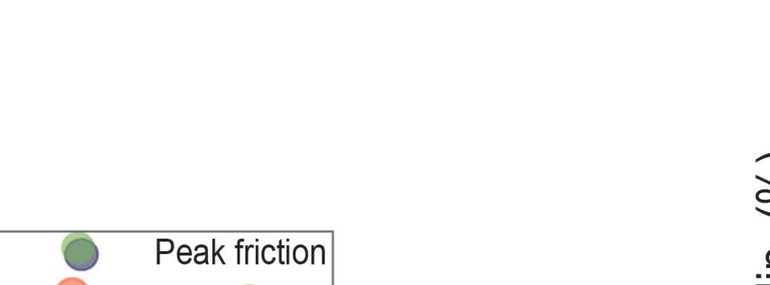

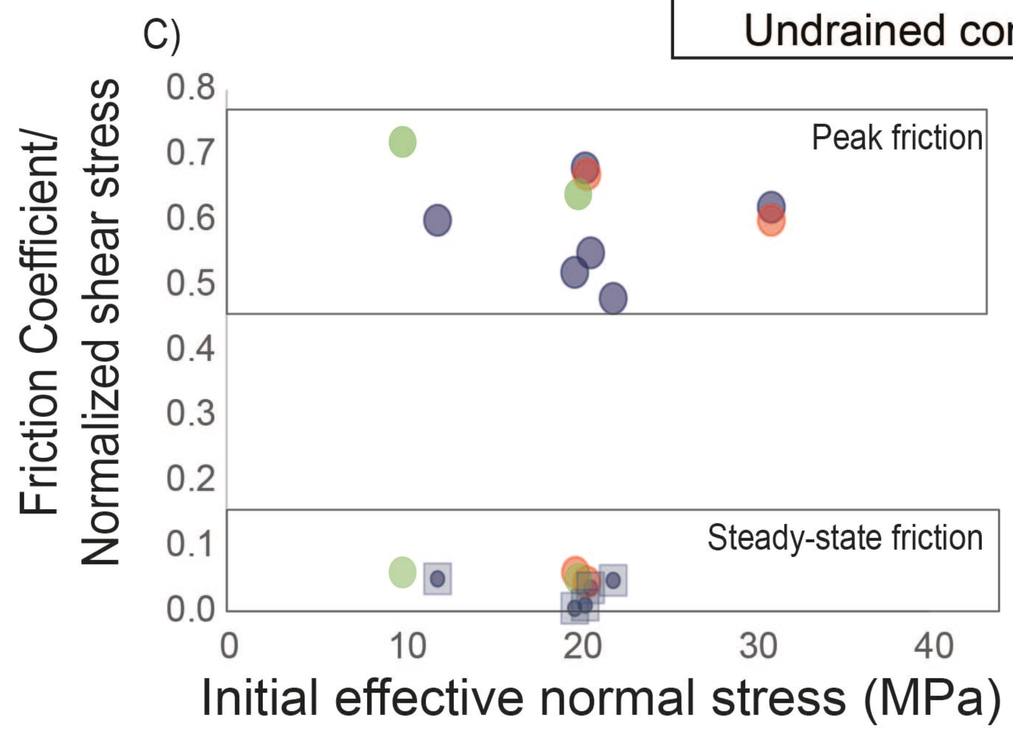

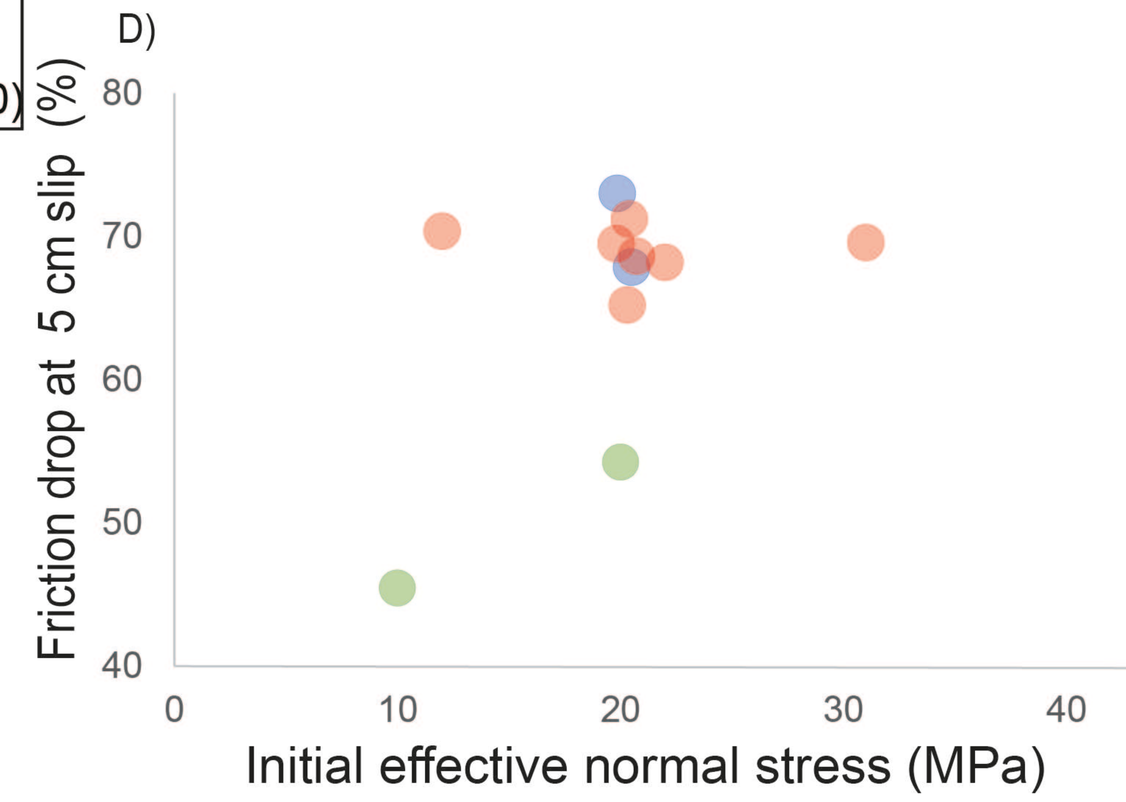

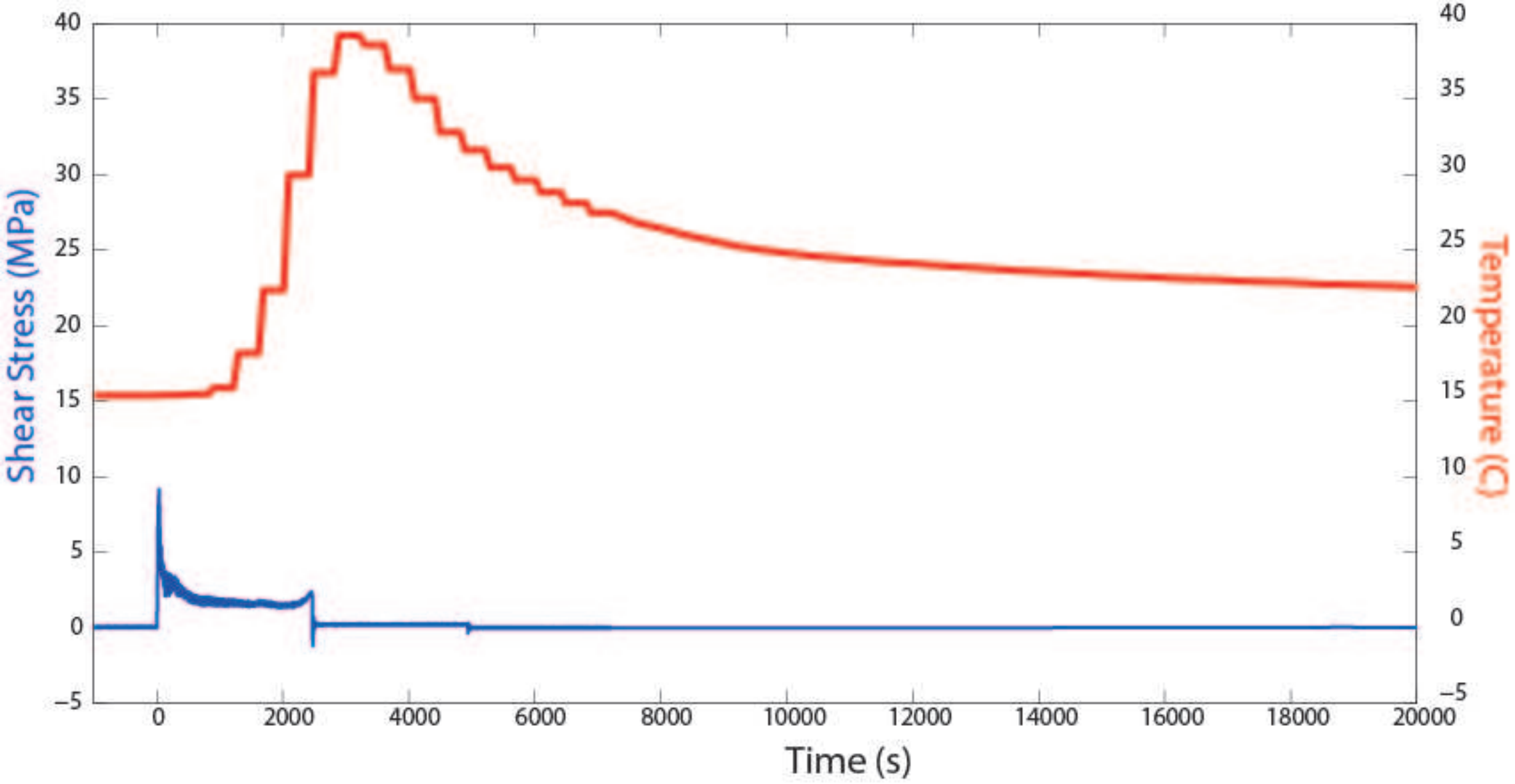
Shear Stress (MPa)
Temperature (C)
Time (s)
40
35
30
25
20
15
10
5
0
−5
0
2000
4000
6000
8000
10000
12000
14000
16000
18000
20000

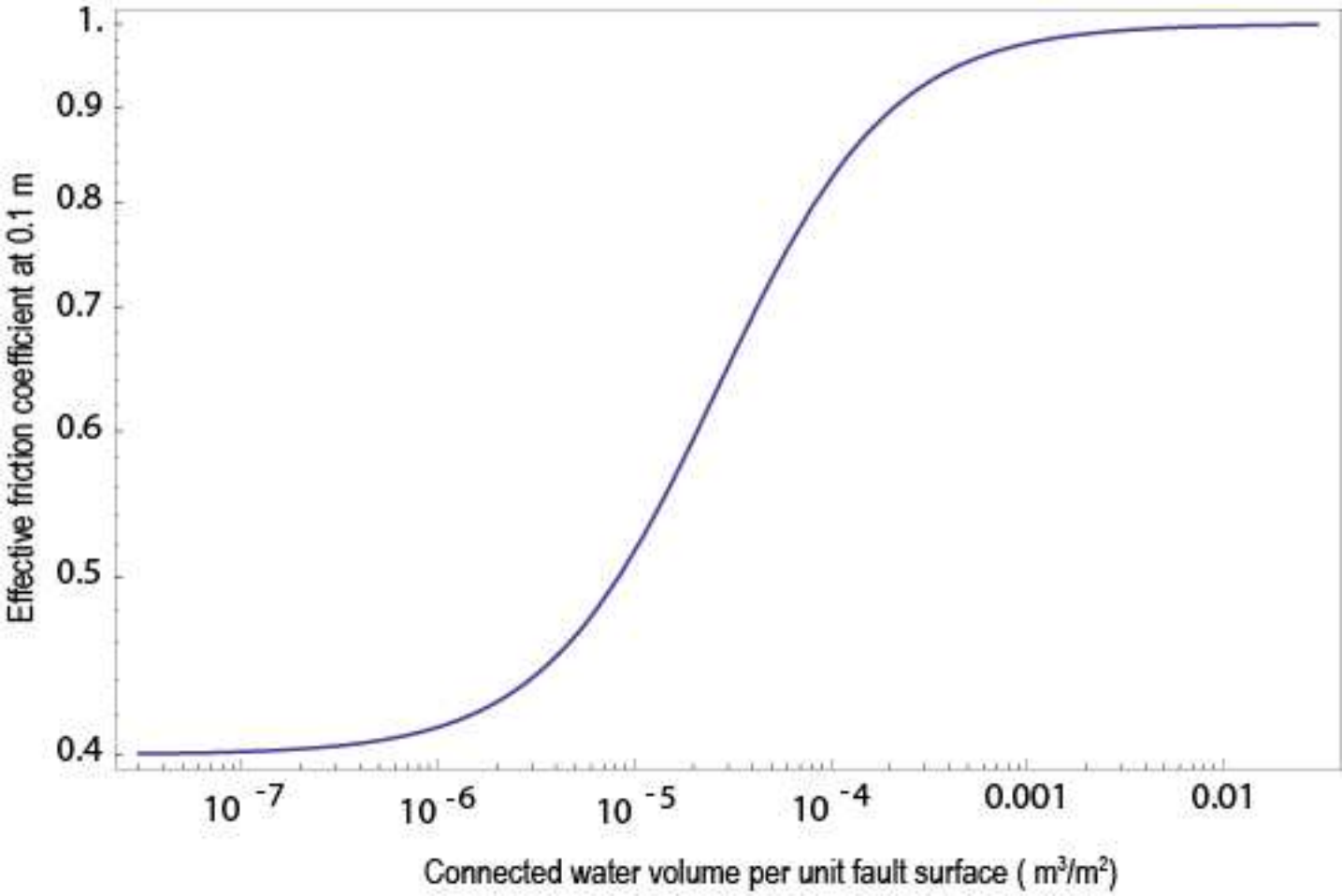
1.
0.9
0.8
0.7
0.6
0.5
0.4
Effective friction coefficient at 0.1 m
10 -7
10 -6
10 -5
10 -4
0.001
0.01
Connected water volume per unit fault surface (m3/m2)